Simulation of the outer radiation belt electron flux decrease during the March 26, 1995, magnetic storm

L. Desorgher,[1] P. Bühler, and A. Zehnder
Paul Scherrer Institut, Villigen, Switzerland

E. O. Flückiger
Physikalisches Institut, Universität Bern, Bern

Abstract. In this paper we study the variation of the relativistic electron fluxes in the Earth's outer radiation belt during the March 26, 1995, magnetic storm. Using observations by the radiation environment monitor (REM) on board the space technology research vehicle (STRV-1b), we discuss the flux decrease and possible loss of relativistic electrons during the storm main phase. In order to explain the observations we have performed fully adiabatic and guiding center simulations for relativistic equatorial electrons in the nonstationary Tsyganenko96 magnetospheric magnetic field model. In our simulations the drift of electrons through the magnetopause was considered as a loss process. We present our model results and discuss their dependence on the magnetospheric magnetic and electric field model, as well as on the prestorm fluxes used in the simulations.

1. Introduction

The outer radiation belt relativistic electron population is known to be highly variable during magnetic storms [*Paulikas and Blake*, 1979; *Baker et al.*, 1986, 1994; *Li et al.*, 1997]. During the main phase the electron fluxes decrease by up to a few orders of magnitude. Then during the recovery phase the fluxes increase to reach levels sometimes higher and sometimes lower than before the storm.

A mechanism invoked to explain the flux decrease during the storm main phase is the adiabatic deceleration of the particles due to the ring current induced magnetic field changes. However, the observational fact that fluxes after the storm are sometimes lower than before suggests that real losses of relativistic electrons from the trapping region happen as well [*Li et al.*, 1997]. This loss of particles is still not understood. A mechanism proposed is the precipitation of the electrons into the atmosphere. Another one is the outward drift of the electrons into the magnetopause [*Thorne and Kennel*, 1971; *Li et al.*, 1997]. Whereas it was never concluded from observations that the precipitation of relativistic electrons into the atmosphere represents a dominant loss process during magnetic storm main phase [*Imhof et al.*, 1991; *Li et al.*, 1997], the importance of the outward drift and loss of electrons into the magnetopause was hardly investigated until now. *Kim and*

Chan [1997] and *Nakamura et al.* [1998] have simulated fully adiabatic variations of equatorial electrons during the storm main phase in nonstationary magnetospheric magnetic field but no loss processes were considered.

In the present work we compute the flux dropout of the outer belt relativistic electron population during the March 26, 1995, magnetic storm by using fully adiabatic and guiding center simulations for equatorial electrons in the nonstationary Tsyganenko96 magnetospheric magnetic field model [*Tsyganenko*, 1995, 1996], and by considering the drift of electrons through the magnetopause as a loss process. Our simulation results are compared to outer radiation belt observations from the radiation environment monitor (REM) aboard the U.K. space technology research vehicle (STRV-1b) [*Bühler et al.*, 1996; *Wells*, 1994].

In section 2, instrumental data used in this study are described. The observations of the outer belt dynamics during the March 26, 1995, magnetic storm are presented in section 3. In section 4, the simulation methods are described, and the results are compared with the observations. The results are discussed in section 5. Finally, conclusions are presented in section 6.

2. Instrument and Data

The REM instrument measures the energy deposit by charged particles into two independent, shielded solid state detectors [*Bühler et al.*, 1996]. For each measurement, data are accumulated typically for 300 s. Both detectors have an opening angle of 90° and are covered with a shielding dome of aluminum such that only electrons with energies $>\sim 1$ MeV and protons with energies $>\sim 35$ MeV are detected. An additional shielding of tantalum on the first detector reduces significantly the penetration of electrons in the relevant energy range (1-10 MeV). For this reason it is called proton detector (p-detector) while the second detector is called electron detector (e-detector). From the count rate ratio between e- and p-detectors, we can deduce the type of the dominant particle population observed by REM.

From June 1994 to September 1998 a REM instrument was in operation aboard the STRV-1b satellite [*Wells*, 1994]. This satellite was moving on a geostationary transfer orbit (GTO), with a period of 10 hours and an inclination of 7°. Because of the large opening angle of the detector, the rotation of STRV-1b (6.5 rpm), and the contribution from the backside of the detector, only omnidirectional information on particle fluxes was possible.

We present STRV-1b REM e-detector count rates as a signature of the relativistic electron population in the outer belt. Those data are plotted versus the *McIlwain* [1961] L shell parameter. This parameter is calculated with the *Tsyganenko* [1989] ($Kp = 0$) magnetospheric magnetic field model plus the International Geomagnetic Reference Field (IGRF95) [*Langel*, 1992].

Solar wind and interplanetary magnetic field data are derived from the solar wind experiment (SWE) [*Ogilvie et al.*, 1995] and the magnetic field investigation (MFI) aboard the Wind spacecraft [*Lepping et al.*, 1995]. Geomagnetic indices were found on the World Wide Web page of the World Data Center C2 for Geomagnetism [*Kamey et al.*, 2000].

3. Observations

Figure 1 shows the variations of the outer electron belt during the March 26, 1995, magnetic storm. In Figure 1a the REM e-detector count rates are plotted versus L for different STRV-1b crossings of the outer belt. The left part corresponds to measurements before and during the storm main phase, and the right one corresponds to the recovery phase of the storm. The hourly *Dst* index is plotted in panel Figure 1b. Each bold section in the *Dst* curve marked by a number delimits the time period corresponding to the count rate profile in Figure 1a labeled by the same number. Figures 1c-1g represent 5-min averages of the solar wind velocity V_{sw}, the proton density of the solar wind N_{prot}, the interplanetary magnetic field (IMF) B_z component in GSM coordinates, the parameter ϵ defined by *Perreault and Akasofu* [1978], and the ring current asymmetry index *Asym* [*Kawasaki and Akasofu*, 1971], respectively. The indices *Asym* and ϵ are used to quantify the substorm activity during this event.

Figure 1

During March 25, 1995, no changes were observed in the solar wind, and the magnetosphere and its radiation belts were quiet. Early on March 26 the solar wind velocity started to increase, reached ~ 500 km/s in the evening of March 27, stayed around this value until the evening of March 29, and then started to decrease. This corotating interaction region (CIR) high-speed solar wind stream sequence [*Tsurutani et al.*, 1995] was the cause of an important magnetic storm when it impinged upon the magnetosphere. First an increase in *Dst* was associated with a solar wind density enhancement which compressed the magnetosphere. Then, promoted by a long-lasting period of high-magnitude southward IMF (see B_z variation), an important magnetic storm main phase developed during which the ring current *Dst* reached, around 1800 UT March 26, a minimum value of $\sim$-100 nT. Note that during the phase with density enhancement and southward IMF, the *Dst* variation was probably the signature of both a ring current injection and a magnetopause compression. After the main phase, *Dst* increased quickly by ~ 60 nT and then recovered slowly. The steep increase of *Dst* is usually explained by the fact that oxygen ions dominate the proton population in the ring current during the main phase but disappear more rapidly [*Kamide et al.*, 1998].

As can be seen in Figure 1a, during the main phase the relativistic electron population of the outer belt decreased over the entire outer belt together with the *Dst* index. The factor between the maximum count rates observed before the main phase (periods 1, 1a, and 2) and around the minimum of *Dst* (period 3) is ~ 50. Looking at the right part of Figure 1a, we see that during the steep *Dst* increase (periods 4 and 5) the count rates increased practically at all L. After this, when *Dst* recovered slowly, the count rates were quite stable for $L < 3.8$ and increased at higher L peaking around $L = 5$. This slow increase took more than 3 days. After the period 9 the outer belt stopped increasing (not shown here). Finally, after the storm the outer belt had a two peak structure. The peak at lower L was probably due to relativistic electrons already there before the storm, and the second peak was probably the signature of a new population. We also note from the comparison of the outer belt at low L before and after the storm that there were clearly fewer particles in this region after the storm.

The count rate dropout during the storm main phase correlates with the decrease of *Dst* and so with a decrease of the magnetic field strength in the relevant part of the magnetosphere. The mechanism usually invoked to explain this observation is adiabatic deceleration [*McIlwain*, 1966, 1996]. If the three adiabatic invariants are conserved, a decrease of the magnetic field induces a deceleration and an outward motion of the particles. Therefore the electron flux decreases. However, many observations have shown lower outer belt fluxes after *Dst* recovery than before the magnetic storm. As we have seen above, this was also the case for the March 26, 1995, magnetic storm at $L < 3.8$. Therefore, beside the reversible adiabatic deceleration mechanism, a loss of radiation belt particles must take place during the magnetic storm. A conceivable mechanism is pitch angle scattering into the loss cone and subsequent absorption in the atmosphere. However, none of the observations have shown that this is the dominant loss process for relativistic electrons during magnetic storms [*Imhof et al.*, 1991; *Li et al.*, 1997] . Another possible loss mechanism is the drift of electrons into the magnetopause, which we attempt to investigate with our simulations.

To explain the increase of the outer belt relativistic population during the recovery phase, it is generally believed that low-energy electrons are injected during substorms and then accelerated to relativistic energy inside the magnetosphere, by a still to be identified acceleration mechanism [*Fujimoto and Nishida*, 1990; *Baker et al.*, 1989; *Boscher et al.,* 2000; *Hudson et al.*, 2000; *Elkington et al.*, 1999; *Li et al.*, 1997; *Liu et al.*, 1999; *Summers et al.*, 1998].

4. Simulations

In our simulations of the March 26, 1995, magnetic storm we consider only equatorial electrons with energies above 0.5 MeV. The flux variations are computed with fully adiabatic and guiding center simulations in a time-varying magnetic field which is driven by solar wind and geomagnetic parameters.

4.1. Magnetospheric Magnetic Field Model

For the variation of the magnetic field during the magnetic storm we used the Tsyganenko96 magnetospheric magnetic field model [*Tsyganenko*, 1995, 1996]. In this model the geomagnetic field is a tilted dipole field. However, in some of our simulations we replaced the centered dipole field by an offset tilted dipole field or by the IGRF95. The magnetospheric field sources are the ring current and the tail current sheet. A magnetopause field is added to the other contributions such that the total magnetic field $\vec{B}$ is confined within the magnetopause. The size of the model magnetopause is a function of the solar wind dynamic pressure $P_{\rm sw}$ such that when $P_{\rm sw}$ increases, the entire magnetosphere is uniformally compressed. The model includes also field-aligned currents and partial penetration of the IMF into the magnetosphere, but we neglect those contributions in our simulation. The model is driven by five time-dependent parameters: the dipole tilt angle Ψ, the Dst index, $P_{\rm sw}$, and the B_z and B_y GSM components of the IMF. The temporal variations of Dst, $P_{\rm sw}$, B_y, and B_z are obtained by interpolating between their hourly values.

In this nonstationary magnetic field we simulate the dynamics of relativistic electrons trapped in the equatorial surface. This surface is the locus of points where the magnetic field magnitude B along a magnetic field line is minimum. When the geomagnetic field is described by the nontilted dipole field, the equatorial surface coincides with the GSM $x-y$ plane. For other geomagnetic field models it is no longer a plane, and it has to be determined numerically.

4.2. Fully Adiabatic Simulation

4.2.1. Method. In the fully adiabatic simulation it is assumed that the magnetic and electric fields vary slowly in comparison with the drift period of a particle. In this case the three adiabatic invariants M, J, and Φ are constants of motion [*Roederer*, 1970].

For equatorial particles, $J = 0$, and only the invariance of M and Φ is taken into account. The energy variation is computed by considering

$$M = \frac{p^2}{2m_0 B} = \text{const}, \tag{1}$$

where $\vec{p}$ is the total momentum and m_0 is the rest mass of the particle. The equatorial drift orbit C of a particle is a curve where B = const. The third invariant Φ represents the magnetic field enclosed in this orbit C. It is given by the integral along C of a potential vector $\vec{A}$ consistent with $\vec{B} = \vec{\nabla} \times \vec{A}$,

$$\Phi = \oint_{\mathrm{C}} \vec{A} \cdot d\vec{l}. \tag{2}$$

An analytical expression of the potential vector $\vec{A}$ was obtained from the analytical description of the magnetospheric magnetic field model [*Tsyganenko*, 1995, 1996]. The integral in (2) is computed numerically. The time variation of the drift orbit and therefore the motion of the particles is deduced from the invariance of Φ.

We assume that particles which drift on the same drift orbit C are equally distributed on it. This implies that the flux of equatorial electrons, $j_{\mathrm{eq}}(E, \Phi, t)$, at time t is a function of the kinetic energy E (and thus of M) and Φ. By considering Liouville's theorem, the relation between particle flux and phase space density, and the invariance of M, we obtain a new constant of motion,

$$\frac{j_{\mathrm{eq}}(E, \Phi, t)}{B} = \text{const}. \tag{3}$$

The variation of the equatorial electron flux is obtained by considering (3) and the invariance of M and Φ [*Roederer*, 1970].

4.2.1.1. Comparison between observations and simulated electron flux: In order to compare simulated electron flux variations with REM observations, the position of STRV-1b for each observation point is associated with the equatorial drift orbit crossing the magnetic field line passing through this satellite position. The third adiabatic invariant Φ corresponding to this drift orbit is computed by using (2). The omnidirectional flux at the STRV-1b position, $J(E, \Phi, t)$, is assumed to be proportional to the equatorial electron flux $j_{\mathrm{eq}}(E, \Phi, t)$. The omnidirectional flux is converted to REM e-detector count rates c by

$$c(\Phi, t) = \int J(E, \Phi) G(E) dE, \qquad (4)$$

where G represents the geometric factor of the e-detector for incident omnidirectional electrons [*Bühler et al.*, 1996]. The simulated count rates c are finally compared with the observed ones.

4.2.1.2. Prestorm fluxes: Prestorm omnidirectional fluxes $J_0(E, \Phi)$ and therefore prestorm equatorial fluxes are deduced from REM measurements during period 1 (see Figure 1). The electron spectra, at each STRV-1b position of period 1, are approximated by an exponential function of energy $J_0(E, \Phi) = F \exp(-E/E_0)$, where the amplitude F and the spectral parameter E_0 are deduced by a fitting procedure [*Bühler et al.*, 1996]. The prestorm fluxes obtained with this method are shown in Figure 2. Figure 2

4.2.2. Results. The results obtained with the fully adiabatic simulation are presented in this section.

4.2.2.1. Motion and energy variation: Fully adiabatic motion and energy variation of equatorial electrons on March 26, 1995, are characterized in Figure 3. For simplicity in this simulation a nontilted dipole is chosen to represent the geomagnetic field. Figure 3

Figure 3a reproduces the *Dst* variation. Figure 3b shows the radial motion at noon and at midnight of electron drift orbits which at 0000 UT cross the noon meridian at 3, 4, and 5 R_{E}. We call these drift orbits C_3, C_4, and C_5, respectively. Figure 3c represents the energy variation of electrons with an initial energy of 1 MeV, drifting on C_3, C_4, and C_5. When *Dst* decreases (increases), the magnetospheric magnetic field decreases (increases) in the inner magnetosphere. Therefore the electrons are decelerated (accelerated), and their drift orbits move outward (inward) as their three adiabatic invariants remain constant. Electrons at larger radial distance move further outward and lose more energy. The altitude of an electron drift orbit is higher at noon than at midnight, owing to the dayside-nightside asymmetry of the magnetospheric magnetic field. As this asymmetry is the result of magnetopause and magnetotail currents, this effect increases with radial distance. At 1400 UT, particles drifting on C_5 encounter the magnetopause where they are considered to be lost from the trapping region.

4.2.2.2. Count rate variations: In the main panel of Figure 4, simulated REM count rates for the pe- Figure 4 riod 1-6, as defined in Figure 1, are compared to observations. For the ease of comparison the Dst time variation and the selected time periods 1-6 are reproduced in the top panel. The solid, short-dashed, and long-dashed lines represent the simulated count rates obtained by considering for the geomagnetic field the IGRF95, the nontilted geomagnetic dipole, and the tilted-offset geomagnetic dipole, respectively. We recall that the McIlwain L values used here are computed by using the Tsyganenko89 model with $Kp = 0$ and the IGRF95. As L is computed always with $Kp = 0$, it does not reflect any change in the magnetospheric magnetic field. It just represents the STRV-1b position, where observed and simulated count rates are compared.

During periods 2, 4, and 5, count rates based on the nontilted geomagnetic dipole and IGRF95 show distinct differences. These differences are characterized by shifts in L without significant changes in the shape and maxima of the count rate profiles. By taking a too simple geomagnetic field, as is obviously the case with the nontilted dipole, we associate STRV-1b to a drift shell too different from reality. Note that there are nearly no differences between the simulations with IGRF95 and with the tilted-offset geomagnetic dipole, showing that the use of the tilted-offset dipole is already a good approximation for the simulation. We will in the following compare the observations to the simulated count rates obtained with IGRF95.

During period 1, STRV-1b REM count rates were used to map the prestorm fluxes, and therefore simulated and observed count rates coincide for $L > 3$. Compared to period 1, the simulated count rate profile during period 2 exhibits small decreases in the maximum value and a slight shift outward while the observed count rates do not change significantly from their prestorm values. The decrease is presumably the effect of the solar wind dynamic pressure increase (see $N_{\rm prot}$ in Figure 1). It seems that the peak in $P_{\rm sw}$ around 0900 UT on March 26, 1995, is the source of an overestimation of the ring current strength in the Tsyganenko96 model. This leads in the simulations to an adiabatic deceleration and outward motion of electrons in the outer belt.

From periods 2 to 3, simulated and observed count rates decrease as the Dst index decreases. During period 3, simulated count rates are smaller than observed count rates for $L < 4.7$ but higher at higher L values. The maxima differ by about a factor 4. The vertical lines in the simulated curves at high L values mark the limit of the trapping region. Above this limit, equatorial electrons drift into the magnetopause and are considered to be lost.

Period 4 corresponds to the magnetic storm phase when the *Dst* index and the different count rates reach their minima. We see clearly that at all L values the fully adiabatic variation gives rise to count rates which are considerably lower than the observed ones. This result confirms that adiabatic deceleration is a major process to explain flux dropout in the outer belt during the magnetic storm main phase. The model predicts a complete loss of electrons above $L = 5.5$ at this time period, which is not the case in reality.

From periods 4 to 5, an increase in *Dst* of ~ 50 nT is accompanied by an increase in the simulated and observed count rates. During period 5, simulated count rates are slightly lower than the observations for $L \leq 3.7$ but higher by a factor 5-10 at higher L. For periods 5 and 6, the vertical lines in the count rate profiles mark the limit between magnetic shells which did not meet the magnetopause during the storm main phase and those which did and lost their electrons. Therefore the simulated count rates have a cutoff at this boundary. The simulated count rates above this limit represent results of the simulation if we do not consider the magnetopause loss. The count rate cutoff is clearly not observed in reality. By using guiding center simulation with a nonstationary convection electric field in the section 4.3, our hope is to induce a diffusion of particles from lower to higher altitudes and therefore to soften this sharp boundary. In section 5, possible reasons for discrepancies between simulation and results will be invoked.

For the rest of March 27-28, *Dst* is fluctuating by less than 10 nT around a value of $\sim$-50 nT, and the simulated count rates exhibit slight variations compared to the magnetic storm main phase (as can be seen by comparing the count rate profiles of periods 5 and 6). Below $L = 4$ the observed count rates remain roughly constant with time while at higher altitude an increase is observed. This increase is not reproduced in the model as no source mechanism for producing relativistic electrons has been considered.

4.2.2.3. Effect of the magnetotail and the magnetopause currents: We also studied the effect of the magnetotail and magnetopause currents of the Tsyganenko96 model on the variations of the outer belt count rates. For this purpose we computed the adiabatic motion of electrons in two modified versions of the Tsyganenko96 model. In the first one we omitted the contribution of the magnetotail, in the second one we omitted the contribution of both the magnetopause and the magnetotail. In Figure 5, results of these sim-

Figure 5

ulations are compared to the simulations obtained with the complete Tsyganenko96 model for period 4.

By comparing the solid bold and thin-dashed lines we see that when the magnetotail is neglected, the count rate dropout is reduced, and the count rate cutoff is at higher L values. As the tail component decreases the magnetic field in the nightside sector, it enhances the deceleration and outward motion of the particles and therefore the flux dropout. By comparing the dashed and dotted lines we see that the presence of magnetopause currents limits the count rate dropout while the count rate cutoff is at higher L values. As the magnetopause currents increase the magnetic field in the dayside magnetosphere, they have the opposite effect on the outer belt dynamics than the magnetotail currents do.

4.2.2.4. Influence of the prestorm spectra: Finally, we also studied the effect of the spectral hardness of the prestorm outer belt electron fluxes on the count rate variations. We have considered exponential prestorm spectra, $J_e = F \exp(-E/E_0)$, with E_0 constant over the entire outer belt. We have selected $E_0 = 1$, 0.5, and 0.25 MeV. The amplitudes F were defined such that the count rates calculated with (4) match the observations during period 1. Simulated REM count rates obtained from these prestorm spectra and from the prestorm spectra defined in Figure 2, by using the full Tsyganenko96 model and IGRF95, are plotted in Figure 6 for period 4. Figure 6

We see that harder spectra give rise to less important count rate decreases. For $L > 3.5$ the simulated count rates obtained with $E_0 = 1$ MeV are much higher than the simulated count rates obtained with the prestorm fluxes deduced from REM measurements. These results illustrate that the proper determination of prestorm spectra is crucial for the simulations.

4.3. Guiding Center Simulations

4.3.1. Method. For the guiding center simulation we take the geomagnetic field as a nontilted dipole field, such that the equatorial surface is the GSM $x-y$ plane. We solve numerically the relativistic guiding center equation for equatorial particles [*Northrup*, 1963],

$$\frac{d\vec{R}}{dt} = \frac{\vec{B}}{B^2} \times (-\vec{E} + \frac{qM}{\gamma}\vec{\nabla}B), \tag{5}$$

where $\vec{R}$ is the guiding center position, γ is the relativistic factor, q is the particle charge, and $\vec{E}$ is the electric field. In (5) the first adiabatic invariant M is still a constant of motion.

The electric field is given by

$$\vec{E} = \vec{E}_{\text{ind}} + \vec{E}_{\text{conv}} + \vec{E}_{\text{cor}}, \tag{6}$$

where $\vec{E}_{\text{ind}}$ represents the electric field induced by the variation of the magnetospheric magnetic field, $\vec{E}_{\text{cor}}$ is the corotation electric field due to Earth's rotation, and $\vec{E}_{\text{conv}}$ is the convection electric field resulting from the interaction of the solar wind with the magnetosphere.

In the equatorial plane where the trajectories are traced, the induced electric field is given by

$$\vec{E}_{\text{ind}} = -\frac{\partial \vec{A}}{\partial t}. \tag{7}$$

Note that we have obtained $\vec{A}$ perpendicular to $\vec{B}$ in the equator to ensure $\vec{E} \perp \vec{B}$.

The convection electric field is derived from a Stern-Volland-type convection electrical potential ϕ_{conv} for which we consider two different models [*Stern*, 1973; *Volland*, 1973]. In a first model we take into account a convection potential based on the model of *Maynard and Chen* [1975],

$$\phi_{\text{conv}} = A(t) r_0 (\frac{r}{r_0})^{\gamma} sin(\phi), \tag{8}$$

where $r_0 = 10.R_{\text{E}}$, r and ϕ are polar coordinates in the equatorial plane, and $A(t)$ is the following function of the Kp index:

$$A(t) = \frac{45}{(1 - 0.159Kp + 0.009Kp^2)^3} V/R_{\text{E}}. \tag{9}$$

The parameter γ is the so-called shielding parameter. When setting $\gamma = 2$, the same shielded convection electric field derived by Maynard and Chen is obtained while when $\gamma = 1$, we obtain a nonshielded duskward and uniform convection electric field. As the amplitude $A(t)$ is a function of the Kp index $\vec{E}_{\text{conv}}$ is varying on a 3-hour timescale. Equatorial electrons which have an energy of 1 MeV in the region $4.5 < L < 5.2$ and which keep their first adiabatic invariant constant have in the region $L < 4.5$ (considering the invariance of M), drift periods around 10-15 min. Therefore, to break significantly the third adiabatic invariant of such particles and to enforce their outward diffusion through the count rate cutoff at $L =\sim 4.5$, a more rapid variation of $A(t)$ is probably needed. For this reason we have modulated the amplitude $A(t)$ as follows. Every 5 min the amplitude jumps from .7 to 1.3 times $A(t)$ and then decreases exponentially with a 2.5-min time constant. In Figure 7a we represent the nonshielded version of the Maynard-Chen convection electric field with modulation of the amplitude $A(t)$. Figure 7

Secondly, we consider representations of $\vec{E}_{\rm conv}$ based on the model of *Chen et al.* [1994]. The convection electrical potential is given by

$$\phi_{\rm conv} = \frac{V_0}{2}(\frac{r}{r^*})^2 \sin(\varphi) + \frac{\delta V(t)}{2}(\frac{r}{r^*})^\gamma \sin(\varphi), \qquad (10)$$

where $V_0 = 50kV$ and $r^* = 8.538\ R_E$. The first term in the right side of (10) defines the quiet time shielded convection electric field while the second term models the variation of the convection electric field during the magnetic storm main phase. The variation of $\delta V(t)$ was taken from Figure 1 of the paper from Chen et al.. The time at which the variation of $\delta V(t)$ starts defines the beginning of the magnetic storm main phase. In our case we fix it to 0700 UT on March 26, 1995. The only difference between our model and the model of Chen et al. is that in (10) they have considered $\gamma = 1$, which gives a nonshielded storm time convection electric field while in our case we have also taken a shielded field with $\gamma = 2$. The nonshielded variant of this field is represented in Figure 7b.

We select at 0000 UT on March 27, 1995, different drift orbits C_i covering efficiently the outer belt, and we compute their corresponding third adiabatic invariant Φ_i and magnetic field magnitude B_i. On each orbit C_i we consider 20 positions equally distributed in azimuth. For each of these positions we compute from the prestorm fluxes plotted in Figure 2 the omnidirectional fluxes of equatorial electrons at different kinetic energies $E_{\rm j}$. This is done by tracing the different time-reversed trajectories of equatorial electrons from 0000 UT on March 27 to 0000 UT on March 26, 1995, constrained by Liouville's theorem (e.g., equation (3)). When a time-reversed trajectory reaches the magnetopause, the corresponding flux is set to zero as no magnetopause sources are considered. The flux corresponding to the same energy $E_{\rm j}$ and the same drift orbit is then averaged over azimuth. Finally, for each selected drift orbit we obtain a new flux $j_{\rm eq}(\Phi_{\rm i}, E_{\rm j})$ as a function of the corresponding third invariant $\Phi_{\rm i}$ and energy $E_{\rm j}$. For the time period after March 27, 1995, the simulated flux of equatorial electrons is deduced from the new flux $j_{\rm eq}(\Phi_{\rm i}, E_{\rm j})$, by considering a fully adiabatic transformation.

4.3.2. Results. In Figure 8 the results obtained for period 5 with the guiding center simulations and the fully adiabatic approximation are compared to the REM observations. The guiding center count rates obtained without convection electric field coincide nearly everywhere with the fully adiabatic count rates. The count rate cutoff obtained with the fully adiabatic simulations is replaced by a rapid decrease of the count

Figure 8

rates in the region $4.5 < L < 4.7$. Then the counts cut off at $L = 4.7$. This equivalence between guiding center and fully adiabatic simulations indicates that the fully adiabatic hypothesis is valid when considering only the induced field. Simulated count rates obtained with the Maynard-Chen convection electric field model (not shown in Figure 8) do not show any significant difference compared to the fully adiabatic results.

Significant differences between results obtained by the guiding center and fully adiabatic simulations are only observed when the nonshielded Chen convection electric field is considered. The convection electric field causes an inward shift of the count rate profile which reduces the difference between the inner edge of the simulated and observed count rates. The cutoff at $L = 4.5$ is now replaced by a slower but still sharp decrease of the count rates for $4.4 < L < 4.7$ followed by a cutoff at $L = 4.7$. Finally, changes around $L = 4.5$ are much too small to significantly reduce the discrepancies between simulations and observations in that region.

5. Discussion

The present study shows that the simulation results depend significantly on the magnetospheric magnetic field model which we have used. *Kim and Chan* [1997] have also computed the fully adiabatic variation of equatorial electrons during a magnetic storm, in a nonstationary magnetospheric model. In their model they considered the nontilted geomagnetic dipole and the *Hilmer and Voigt* [1995] azimuthally symmetric ring current. The shape and the strength of the ring current were varying during the storm as a function of Dst. For a variation of Dst from 0 to -100 nT they obtained an outward motion of equatorial electrons significantly smaller than what resulted from our simulations. A possible explanation for this difference could be that the ring current strength in the Tsyganenko96 model is overestimated. This would explain the fact that during the magnetic storm main phase of March 26, 1995, our fully adiabatic variation gives rise to a count rate decrease and outward motion of the outer belt inner edge which is larger than what was observed.

We have also shown that the presence of the magnetopause currents reduces the outward motion, deceleration, and flux decrease of equatorial electrons during the main phase while the presence of the magnetotail currents has the opposite effect. *Kim and Chan* [1997] have also considered the effect of magnetopause and magnetotail current magnetic fields given by the model from *Ding et al.* [1996]. They found that the outward motion of drift orbits, the particle deceleration, and the flux decrease as induced by the ring current variation are reduced when magnetopause and magnetotail currents are considered. They attributed this effect mainly to the magnetopause currents. The influence of the magnetotail currents was not investigated separately. Our results show that the magnetotail currents may have a significant effect on the fully adiabatic variation of equatorial electrons.

We have also shown that the results of the simulations depend crucially on the prestorm spectra. As illustrated in Figure 6, prestorm exponential spectral indices $E_0 = 1$ MeV and $E_0 = 0.5$ MeV give rise to count rates much higher than the count rates obtained with the prestorm spectra defined in Figure 2. Such values for E_0 reduce the overall difference between simulations and observations during the minimum Dst period.

Nakamura et al. [1998] have also simulated the fully adiabatic variation of equatorial electrons and studied the effect of the prestorm spectra. They considered a magnetospheric magnetic field model based on a nontilted geomagnetic dipole and the azimuthally symmetric ring current model developed by *Schulz* [1997]. They selected two prestorm exponential spectra with $E_0 = 1$ MeV and $E_0 = 0.4$ MeV and obtained a dependence of the flux decrease on the spectral hardness similar to the one obtained in our simulations. These E_0 values correspond to the minimum and maximum of the exponential index E_0 obtained by *Baker et al.* [1996] from outer belt electron measurements with the Solar, Anomalous, and Magnetospheric Particle Explorer (SAMPEX). The NASA AE8 Min/Max model electron spectra [*Vette*, 1991] can be approximated, in the energy range $1 - 5$ MeV, by exponential spectra with $0.4 < E_0 < 1$ MeV. In our study the electron spectra were clearly softer than SAMPEX and AE8 spectra, as we obtained roughly 0.4 MeV $< \mathrm{E}_0 <$ 0.25 MeV from REM observations.

It is clear that a loss mechanism is also needed as observed count rates do not recover to their prestorm values after some magnetic storms. In our simulations we have considered the drift of electrons into the magnetopause as a loss process. For our fully adiabatic simulation this loss process leads during the recovery phase to a count rate cutoff at $L \sim 4.5$. Although this cutoff represents an important loss of particles, comparisons with the data do not lead to the conclusion that the drift of the electrons into the magnetopause is the relevant loss mechanism for the radiation belt electrons during magnetic storms. Indeed, the measurements do not show a count rate cutoff. Moreover, the simulated count rates during the recovery phase are higher than the observations below the cutoff.

We have tried to reduce these discrepancies by using guiding center simulations and by considering induced, corotation, and convection electric fields. The idea was to induce an outward diffusion of the electrons across the L cutoff by using a sufficiently high and variable convection electric field.

Significant differences between results obtained with the guiding center and fully adiabatic simulations are only observed when the nonshielded *Chen et al.* [1994] convection electric field model is considered. The fully adiabatic simulated count rate cutoff at $L = 4.5$ is replaced by a sharp count rate decrease in the region $4.4 < L < 4.7$ and a count rate cutoff at $L = 4.7$. The simulated count rates are still much higher than those in the observations for the region $3.5 < L < 4.5$.

The 5-min periodic modulation of the amplitude in the Maynard-Chen convection electric field does not lead to significant diffusion of the electrons. It is probable that only particles whose drift motions are in resonance with the periodic variation of the convection electric field diffuse radially. By choosing an aperiodic variation of the electric field as in the Chen model, particles with different drift periods could encompass efficient variation of their third invariant. In conclusion, our guiding center simulations do not reduce significantly the main discrepancies between fully adiabatic simulations and observations.

Instead of using guiding center simulations, we could solve directly a radial diffusion equation. To check if the results of such an approach would be significantly different from our simulations, we have solved for equatorial electrons the following equation:

$$\frac{\partial f}{\partial t} = \frac{\partial}{\partial \Phi}\left(D_{\Phi\Phi}\frac{\partial f}{\partial \Phi}\right) - \frac{f}{\tau}, \tag{11}$$

where $f = f(M, \Phi, t)$ is the phase space density of equatorial electrons and $D_{\Phi\Phi}$ represents the radial diffusion coefficient. The parameter τ defines the mean lifetime of particle for the pitch angle scattering loss process.

We have set $D_{\Phi\Phi}$ and τ to the values deduced by *Selesnick et al.* [1997]. These authors have reproduced in a dipole field geometry the radial diffusion and long-term loss of the outer belt 3- to 8-MeV electrons observed during the geomagnetically quiet spring of 1996. In our case we used these coefficients to compute the variation of $E > 1$ MeV equatorial electrons, during the March 26, 1995, magnetic storm, utilizing the Tsyganenko96 model plus the IGRF95. The prestorm fluxes as given in Figure 2 were considered. During the entire storm we have set $f(M, \Phi, t) = 0$ below the outer belt inner boundary and outside the trapping region delimited by the nonstationary magnetopause. As the diffusion is enhanced during a magnetic storm main phase, it is probable that the value of $D_{\Phi\Phi}$ used by *Selesnick et al.* [1997] is underestimated for such an active period. Therefore we have also considered $D_{\Phi\Phi}$ 10 times higher than that in their simulations. We refer to weak and strong diffusion for the respective simulations.

The results are presented in Figure 9 for period 5. The mean lifetimes τ used by *Selesnick et al.* [1997] were much higher than the typical magnetic storm timescale to give rise to a significant loss of electrons during the main phase. Therefore, for these values of τ our simulation is similar to a simulation without the loss term $-f/\tau$ in (11). We see that for the weak diffusion the simulated count rates coincide nearly everywhere with the fully adiabatic simulated count rates. The only difference is that the sharp cutoff in the fully adiabatic case is replaced by a rapid decrease in the region $4.4 < L < 4.7$. When strong diffusion is considered, a net inward radial diffusion produces at $L \leq 4.1$ higher fluxes than the ones obtained with the adiabatic variation. Also, the count rate cutoff is replaced by a decrease of the count rates extending over the region $4.4 < L < 5.2$. Although better storm time radial diffusion coefficients corresponding to the Tsyganenko96 model and IGRF95 for magnetic storm period could be considered, it is not probable that a radial diffusion equation will reduce significantly the main discrepancies obtained between simulated and observed count rates.

Figure 9

Our simulations were made only for equatorial electrons. Inclusion of nonequatorial electrons would introduce a drift shell splitting effect [*Roederer*, 1970]. This effect is higher at higher altitude as the asymmetry of the magnetic field gets higher with altitude. This effect could change considerably the position of the count rate cutoff.

In our simulations we have considered that all the electrons which drift through the magnetopause are lost from the trapping region. It is probable that the magnetopause is much more complex than a simple absorber. It could be possible that some electrons scatter back when they encounter the magnetopause and therefore stay trapped in the magnetosphere. Moreover, the magnetopause could be also considered as a source.

We have also neglected other possible sources of relativistic electrons in the outer belt such as the injection and inward transport/acceleration of electrons from the outer region [*Brautigam and Albert*, 2000] and any possible internal acceleration mechanism of outer belt electrons to relativistic energies [*Fujimoto and Nishida*, 1990; *Baker et al.*, 1989; *Boscher et al.,* 2000; *Hudson et al.*, 2000; *Elkington et al.*, 1999; *Li et al.*, 1997; *Liu et al.*, 1999; *Summers et al.*, 1998]. By taking into account such processes, the count rate cutoff would certainly disappear in the simulation results.

The simulated count rates in the region $3.5 < L < 4.5$ during period 5 may be reduced to a level similar to that of the observations, by taking into account an enhanced precipitation of the electrons into the atmosphere by pitch angle diffusion during a magnetic storm [*Thorne and Kennel*, 1971; *Li et al.*, 1997]. This could be obtained by reducing τ in (11). However, by modeling the pitch angle loss in such a way, it is assumed that radial diffusion and pitch angle scattering are decoupled. In reality, this is not the case, and a more complex diffusion equation has to be considered. Multidimensional diffusion and convection-diffusion models of radiation belt electrons exist but have been worked out so far only for the geomagnetic dipole field [*Bourdarie et al.*, 1997; *Boscher et al.*, 2000]. As an improvement, such diffusion models should be implemented in a more realistic, nonstationary magnetic field model such as that used in this work.

6. Summary and Conclusions

The aim of our simulations with the nonstationary Tsyganenko96 magnetospheric magnetic field model was to study the flux decrease and loss of outer belt relativistic electrons during the March 26, 1995, magnetic storm. The drift of electrons through the magnetopause was considered as a loss process. We have shown that the influence of the magnetospheric magnetic field model and of the prestorm particle spectra on the simulation results is important.

During the storm main phase, the adiabatic deceleration leads to an outer belt electron flux decrease more important than that in the observations. It confirms that adiabatic variation of electrons is a crucial process during the magnetic storm main phase.

The drift of electrons through the magnetopause leads to a count rate cutoff at $L > 4.5$ during the recovery phase. This result shows that the drift of electrons through the magnetopause could be an important loss mechanism of outer belt electrons during a magnetic storm.

However, the count rate cutoff does not appear in the observations, and below this cutoff the simulated count rates are lower than the observed one. The consideration of different convection electric field models in the simulations does not improve the results compared to the observations. The reasons for the discrepancies between the results and the observations are probably that we have modelized the magnetopause as a simple absorber, that we have neglected the pitch angle diffusion process, and that we did not consider any source process.

An improvement of the model would be certainly to solve a multidiffusion equation in a realistic, nonstationary magnetospheric magnetic field as described, for example, by the Tsyganenko96 model. It would permit taking into account adiabatic effects, as well as radial and pitch angle diffusion processes. In such a model both the precipitation of electrons into the atmosphere and their drift into the magnetopause are considered as loss processes. Source processes should also be included.

Acknowledgments. This study was supported by ESA/ESTEC/WMA Technology Research contract 11108/94/NL/JG(SC) and in part from the Swiss National Science Foundation, grants 2000-050697.97 and 2000-057175.99.

Michel Blanc thanks Daniel Boscher and Mary Hudson for their assistance in evaluating this paper.

References

Baker, D. N., J. B. Blake, R. W. Klebesadel, and P. R. Higbie, Highly relativistic electrons in the Earth's magnetosphere, 1, Lifetimes and temporal history 1979-1984, *J. Geophys. Res., 91*, 4265, 1986.

Baker, D. N., J. B. Blake, L. B. Callis, R. D. Belian, and T. E. Cayton, Relativistic electrons near geostationary orbit: Evidence for internal magnetospheric acceleration, *Geophys. Res. Lett., 16*, 559, 1989.

Baker, D. N., J. B. Blake, L. B. Callis, J. R. Cummings, D. Hovestadt, S. Kanekal, B. Blecker, R. A. Mewaldt, and R. D. Zwickl, Relativistic electron acceleration and decay time scales in the inner and outer radiation belts: SAMPEX, *Geophys. Res. Lett., 21*, 409, 1994.

Baker, D. N., J. B. Blake, L. B. Callis, J. R. Cummings, D. Hovestadt, S. Kanekal, B. Klecker, R. A. Mewaldt, and R. Nakamura, New magnetospheric results from the SAMPEX mission, *AIP Conf. Proc., 38*, 1655, 1996.

Boscher, D., S. Bourdarie, R. Thorne, and B. Abel, Influence of the wave characteristics on the electron radiation belt distribution, *Adv. Space Res., 26*(1), 163, 2000.

Bourdarie, S., D. Boscher, T. Beutier, J.-A. Sauvaud, and M. Blanc, Electron and proton radiation belt dynamic simulations during storm periods: A new asymmetric convection-diffusion model, *J. Geophys. Res., 102*, 17,541, 1997.

Brautigam, D. H., and J. M. Albert, Radial diffusion analysis of outer radiation belt electrons during the October 9, 1990, magnetic storm, *J. Geophys. Res., 105*, 291, 2000.

Bühler, P., S. Ljungfelt, A. Mchedlishvili, N. Schlumpf, A. Zehnder, L. Adams, E. Daly, and R. Nickson, Radiation environment monitor, *Nucl. Instrum. Methods Phys. Res., Sect. A, 368*, 825, 1996.

Chen, M. W., L. R. Lyons, and M. Schulz, Simulations of phase space distributions of storm time proton ring current, *J. Geophys. Res., 99*, 5745, 1994.

Ding, C., T. W. Hill, and F. R. Toffoletto, Improvements of the Toffoletto-Hill open magnetosphere model, in *Physics of Space Plasmas (1995)*, no.14, edited by T. Chang and J. R. Jasperse, p.639, MIT Press, Cambridge, Mass., 1996.

Elkington, S. R., M. Hudson, and A. Chan, Acceleration of relativistic electrons via drift-resonant interaction with toroidal-mode Pc-5 ULF oscillations, *Geophys. Res. Lett., 26*, 3273, 1999.

Fujimoto, M., and A. Nishida, Energization and anisotropization of energetic electrons in the Earth's radiation belt by the recirculation process, *J. Geophys. Res., 95*, 4265, 1990.

Hilmer, R. V., and G. H. Voigt, A magnetospheric magnetic field model with flexible current systems driven by independent physical parameters, *J. Geophys. Res., 100*, 5613, 1995.

Hudson, M. K., S. R. Elkington, J. G. Lyon, and C. C. Goodrich, Increase in relativistic electron flux in the inner magnetosphere: ULF wave mode structure, *Adv. Space Res., 25*(12), 2327, 2000.

Imhof, W. L., H. D. Voss, J. Mobilia, D. W. Datlowe, J. P. McGlennon, and D. N. Baker, Relativistic electron enhancements: Simultaneous measurements from synchronous and low altitude satellites, *Geophys. Res. Lett., 18*, 397, 1991.

Kamei, T., et al., Geomagnetic Data Service, *http://swdcdb-.kugi.kyoto-u.ac.jp/wdc/Sec3.html*, World Data Cent. C2 for Geomagn., Kyoto, 2000.

Kamide, Y., et al., Current understanding of magnetic storms: Storm-substorm relationships, *J. Geophys. Res., 103*, 17,705, 1998.

Kawasaki, K., and S.-I. Akasofu, Low-latitude DS component of geomagnetic storm field, *J. Geophys. Res., 76*, 2396, 1971.

Kim, H.-J., and A. A. Chan, Fully adiabatic changes in storm time relativistic electron fluxes, *J. Geophys. Res., 102*, 22,107, 1997.

Langel, R. A., International Geomagnetic Reference Field: The sixth generation *J. Geomagn. Geoelectr., 44*, 679, 1992.

Lepping, R. P., M. H. Acuna, L. F. Burlaga, W. M. Farrell, J. A. Slavin, K. H. Schatten, F. Mariani, N. F. Ness, F. M. Neubauer, and Y. C. Whang, The wind magnetic field investigation, *Space Sci. Rev., 71*, 207, 1995.

Li, X., D. N. Baker, M. Temerin, T. E. Cayton, E. G. D. Reeves, R. A. Christensen, J. B. Blake, M. D. Looper, R. Nakamura, and S. G. Kanekal, Multisatellite observations of the outer zone electron variation during the November 3-4, 1993, magnetic storm, *J. Geophys. Res., 102*, 14,123, 1997.

Liu, W. W., G. Rostoker, and D. N. Baker, Internal acceleration of relativistic electrons by large-amplitude ULF pulsations, *J. Geophys. Res., 104*, 17,391, 1999.

Maynard, N. C., and A. J. Chen, Isolated cold plasma regions: Observations and their relation to possible production mechanisms, *J. Geophys. Res., 80*, 1009, 1975.

McIlwain, C. E., Coordinates for mapping the distribution of magnetically trapped particles, *J. Geophys. Res., 66*, 3681, 1961.

McIlwain, C. E., Ring current effects on trapped particles, *J. Geophys. Res., 71*, 3623, 1966.

McIlwain, C. E., Processes acting upon outer zone electrons, in *Radiation Belts: Models and Standards*, *Geophys. Monogr. Ser.*, vol. 97, edited by J. F. Lemaire, D. Heynderickx, and D. N. Baker, p.15, AGU, Washington, D.C., 1996.

Nakamura, R., K. Kamei, Y. Kamide, D. N. Baker, J. B. Blake, and M. Looper, SAMPEX observations of storm-associated electron flux variations in the outer radiation belt, *J. Geophys. Res., 103*, 26,261, 1998.

Northrup, T. G., *The Adiabatic Motion of Charged Particles*, Wiley-Interscience, New York, 1963.

Ogilvie, K. W., et al., SWE: A comprehensive plasma instrument for the WIND spacecraft, *Space Sci. Rev., 71*, 55, 1995.

Paulikas, G. A., and J. B. Blake, Effects of the solar wind on magnetospheric dynamics: Energetic electrons at the synchronous orbit, in *Quantitative Modeling of Magnetospheric Processes.*, *Geophys. Monogr. Ser.*, vol. 21, edited by W. P. Olsen, p. 180, AGU, Washington, D. C.,

1979.
Perreault, P., and S.-I. Akasofu, A study of geomagnetic storms, *Geophys. J. R. Astron. Soc., 54*, 547, 1978.
Roederer, J. G., *Dynamics of Geomagnetically Trapped Radiation*, Springer-Verlag, New York, 1970.
Schulz, M., Direct influence of ring current on auroral oval diameter, *J. Geophys. Res., 102*, 14,149, 1997.
Selesnick, R. S., J. B. Blake, W. A. Kolasinski, and T. A. Fritz, A quiescent state of 3 to 8 MeV radiation belt electrons, *Geophys. Res. Lett., 24*, 1343, 1997.
Stern, D. P., A study of the electric field in an open magnetospheric model, *J. Geophys. Res., 78*, 7292, 1973.
Summers, D., R. M. Thorne, and F. Xiao, Relativistic theory of wave-particle resonant diffusion with application to electron acceleration in the magnetosphere, *J. Geophys. Res., 103*, 20,487, 1998.
Thorne, R. M., and C. F. Kennel, Relativistic electron precipitation during magnetic storm main phase, *J. Geophys. Res., 76*, 4446, 1971.
Tsurutani, B. T., W. D. Gonzales, A. L. C. Gonzales, F. Tang, J. K. Arballo, and M. Okada, Interplanetary origin of geomagnetic activity in the declining phase of the solar cycle, *J. Geophys. Res., 100*, 21,717, 1995.
Tsyganenko, N. A., A magnetospheric magnetic field model with a warped tail current sheet, *Planet. Space Sci., 37*, 5, 1989.
Tsyganenko, N. A., Modeling the Earth's magnetospheric magnetic field confined within a realistic magnetopause, *J. Geophys. Res., 100*, 5599, 1995.
Tsyganenko, N. A., Effects of the solarwind conditions on the global magnetospheric configuration as deduced from data-based field models, *in Proceedings of 3rd International Conference on Substorms (ICS-3), Versailles, France, 12-17 May 1996, Eur. Space Agency Spec. Publ., ESA SP-389*, 181, 1996.
Vette, J. I., The AE-8 trapped electron environment, *Rep. WDC-A- R&S 91-24*, Natl. Space Sci. Data Cent., Greenbelt, Md., 1991.
Volland, H., A semiempirical model of large-scale magnetospheric electric fields, *J. Geophys. Res., 78*, 171, 1973.
Wells, N., The Space Technology Research Vehicles STRV-1a and STRV-1b: First in-orbit results, paper presented at 8th Annual Conference on Small Satellites, AIAA/ Utah State University, Logan, Utah, 1994.

L. Desorgher, and E. O. Flückiger Physikalisches Institut, Universität Bern, Sidlerstrasse 5, Ch-3012 Bern, Switzerland. (e-mail: desorgher@phim.unibe.ch; flueckiger@phim.unibe.ch)

P. Bühler, and A. Zehnder, Paul Scherrer Institut, CH-5232 Villigen PSI, Switzerland. (e-mail: buehler@psi.ch; zehnder@psi.ch)

(Received December 2, 1999; revised March 31, 2000; accepted April 4, 2000.)

[1]Also at Physikalisches Institut, Universität Bern, Bern.

Paper number 2000JA900060.

0148-0227/00/2000JA900060$09.00

Figure 1. Time variation of the outer electron belt and of different solar wind and geomagnetic parameters for the period March 25-31, 1995. (a) Radiation environment monitor (REM) electron detector count rates versus L, for different outer radiation belt crossings by the STRV-1b satellite. (b) Hourly Dst index. A bold section in the Dst curve marked by a given number delimits the time period of the count rate profile marked by the same number in Figure 1a. (c-g) Five-minute averages of the solar wind velocity $V_{\rm sw}$, the solar wind proton density $N_{\rm prot}$, the interplanetary magnetic field (IMF) B_z component in GSM coordinates, the Akasofu-Perreault parameter ϵ and the ring current asymmetry index $Asym$.

Figure 1. Time variation of the outer electron belt and of different solar wind and geomagnetic parameters for the period March 25-31, 1995. (a) Radiation environment monitor (REM) electron detector count rates versus L, for different outer radiation belt crossings by the STRV-1b satellite. (b) Hourly Dst index. A bold section in the Dst curve marked by a given number delimits the time period of the count rate profile marked by the same number in Figure 1a. (c-g) Five-minute averages of the solar wind velocity $V_{\rm sw}$, the solar wind proton density $N_{\rm prot}$, the interplanetary magnetic field (IMF) B_z component in GSM coordinates, the Akasofu-Perreault parameter ϵ and the ring current asymmetry index $Asym$.

Figure 2. Spectral parameter E_0 and amplitude F of the prestorm exponential spectra used in our simulations, versus L values. These parameters were deduced from the REM count rates obtained during the period labeled by 1 in Figure 1.

Figure 2. Spectral parameter E_0 and amplitude F of the prestorm exponential spectra used in our simulations, versus L values. These parameters were deduced from the REM count rates obtained during the period labeled by 1 in Figure 1.

Figure 3. Motion and energy variation of equatorial electrons during March 26, 1995, as obtained with the fully adiabatic simulation in the Tsyganenko96 model. In this case the geomagnetic field is represented by a nontilted dipole field. (a) Dst index. (b) Radial motion at noon (solid line) and midnight (dashed line) of drift orbits crossing the noon meridian at a distance $R = 3$, 4, and 5 R_E, at 0000 UT on March 26, 1995. (c) Energy variation of electrons moving on these drift orbits, with an initial energy of 1 MeV.

Figure 3. Motion and energy variation of equatorial electrons during March 26, 1995, as obtained with the fully adiabatic simulation in the Tsyganenko96 model. In this case the geomagnetic field is represented by a nontilted dipole field. (a) Dst index. (b) Radial motion at noon (solid line) and midnight (dashed line) of drift orbits crossing the noon meridian at a distance $R = 3$, 4, and 5 R_E, at 0000 UT on March 26, 1995. (c) Energy variation of electrons moving on these drift orbits, with an initial energy of 1 MeV.

Figure 4. Comparisons between observed and fully adiabatic simulated REM count rates, for the periods 1-6, as defined in Figure 1. The simulated count rates are obtained by using the Tsyganenko96 model with three different representations of the geomagnetic field: the IGRF95, the tilted-offset geomagnetic dipole (TilDip), and the nontilted geomagnetic dipole (NoTiltDip).

Figure 4. Comparisons between observed and fully adiabatic simulated REM count rates, for the periods 1-6, as defined in Figure 1. The simulated count rates are obtained by using the Tsyganenko96 model with three different representations of the geomagnetic field: the IGRF95, the tilted-offset geomagnetic dipole (TilDip), and the nontilted geomagnetic dipole (NoTiltDip).

Figure 5. Fully adiabatic simulated count rates for period 4 in Figure 1, obtained by omitting in the Tsyganenko96 model either the magnetotail current contribution (long-dashed line) or both the magnetotail and magnetopause current contributions (short-dashed line). For reference the simulated count rates obtained when considering all the contribution of the Tsyganenko96 model are plotted in a solid line as in Figure 4.

Figure 5. Fully adiabatic simulated count rates for period 4 in Figure 1, obtained by omitting in the Tsyganenko96 model either the magnetotail current contribution (long-dashed line) or both the magnetotail and magnetopause current contributions (short-dashed line). For reference the simulated count rates obtained when considering all the contribution of the Tsyganenko96 model are plotted in a solid line as in Figure 4.

Figure 6. Fully adiabatic simulated count rates for period 4 in Figure 1, obtained from four different prestorm exponential spectra by considering the Tsyganenko96 model plus the IGRF95. The solid bold line corresponds to the REM prestorm spectra plotted in Figure 2. The three dashed lines were obtained from prestorm exponential spectra with exponential index E_0 =0.5, 1, and 2 MeV over the entire outer belt.

Figure 6. Fully adiabatic simulated count rates for period 4 in Figure 1, obtained from four different prestorm exponential spectra by considering the Tsyganenko96 model plus the IGRF95. The solid bold line corresponds to the REM prestorm spectra plotted in Figure 2. The three dashed lines were obtained from prestorm exponential spectra with exponential index E_0 =0.5, 1, and 2 MeV over the entire outer belt.

Figure 7. Time variation from 0600 to 2100 UT on March 26, 1995, of the azimuthal component at 5 R_E at noon of different convection electric field models used for the guiding center simulation. (a) Nonshielded Maynard-Chen model with 5-min periodic modulation of the amplitude. (b) Nonshielded Chen model.

Figure 7. Time variation from 0600 to 2100 UT on March 26, 1995, of the azimuthal component at 5 R_E at noon of different convection electric field models used for the guiding center simulation. (a) Nonshielded Maynard-Chen model with 5-min periodic modulation of the amplitude. (b) Nonshielded Chen model.

Figure 8. Guiding center simulated count rates for period 5 in Figure 1, obtained by considering no convection electric field (short-dashed lines) and by considering the nonshielded Chen convection electric field model (long-dashed lines). Comparison with fully adiabatic simulated (solid bold line) and observed (solid thin line) count rates is presented.

Figure 8. Guiding center simulated count rates for period 5 in Figure 1, obtained by considering no convection electric field (short-dashed lines) and by considering the nonshielded Chen convection electric field model (long-dashed lines). Comparison with fully adiabatic simulated (solid bold line) and observed (solid thin line) count rates is presented.

Figure 9. Radial diffusion simulated count rates obtained for period 5 in Figure 1. The long- and short-dashed lines correspond to the strong and weak diffusions respectively (see details in text). Comparison with fully adiabatic simulated (solid bold line) and observed (solid thin line) count rates is presented.

Figure 9. Radial diffusion simulated count rates obtained for period 5 in Figure 1. The long- and short-dashed lines correspond to the strong and weak diffusions respectively (see details in text). Comparison with fully adiabatic simulated (solid bold line) and observed (solid thin line) count rates is presented.

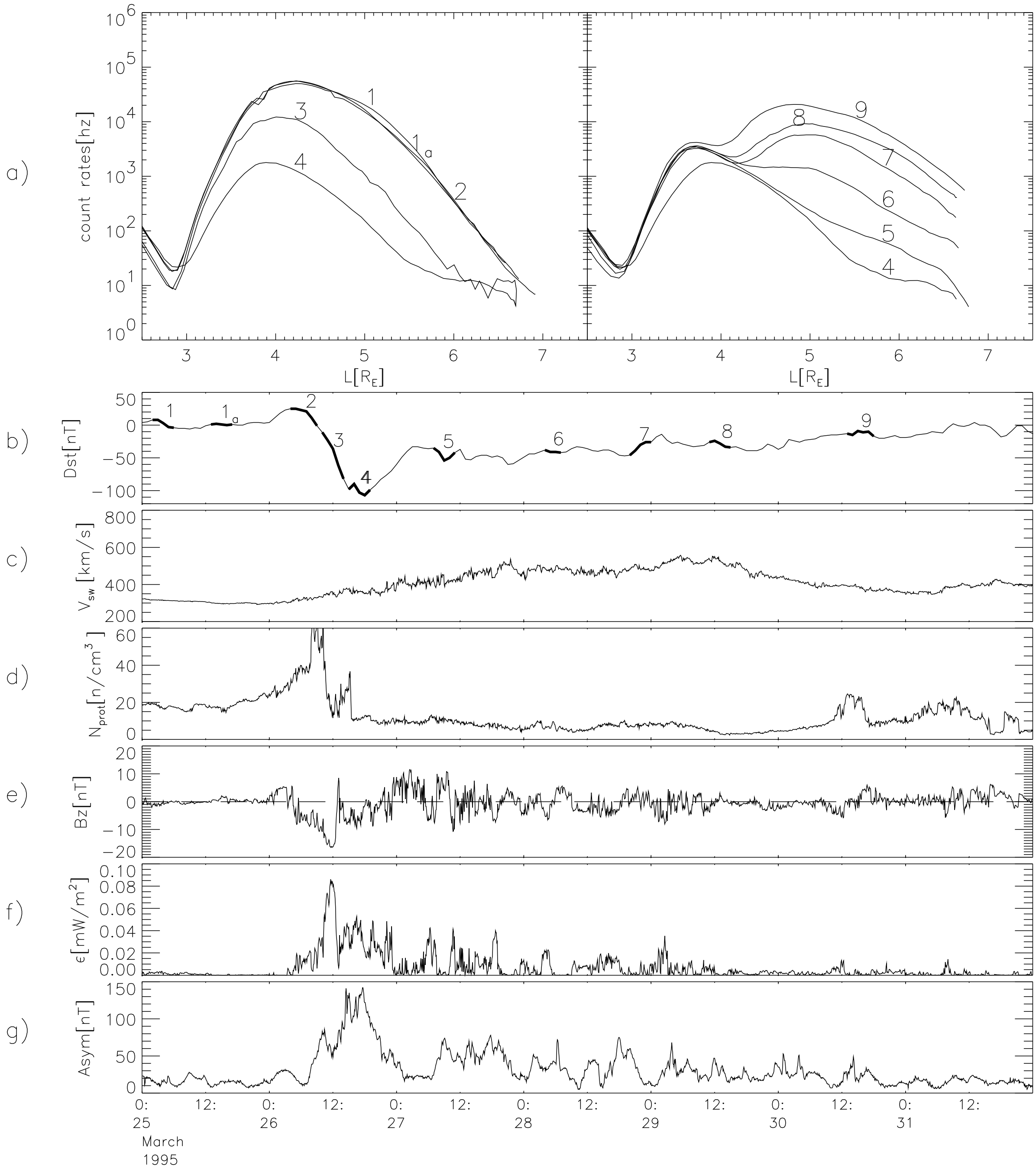

a)
count rates[hz]
L[R_E]
1
1a
2
3
4
5
6
7
8
9
b)
Dst[nT]
c)
V_sw [km/s]
d)
N_prot [n/cm^3]
e)
Bz[nT]
f)
ε[mW/m^2]
g)
Asym[nT]
March
1995

Figure 1

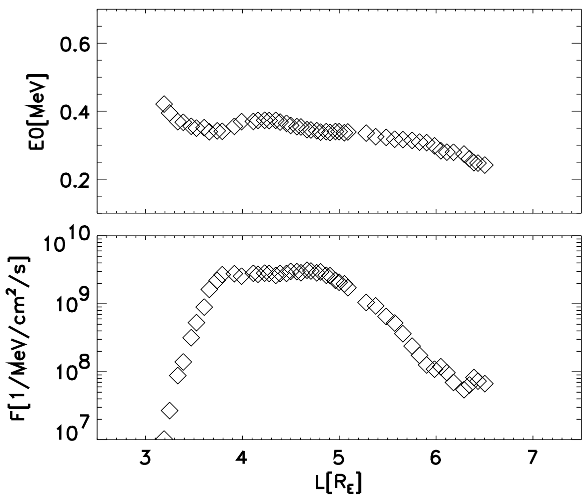

Figure 2

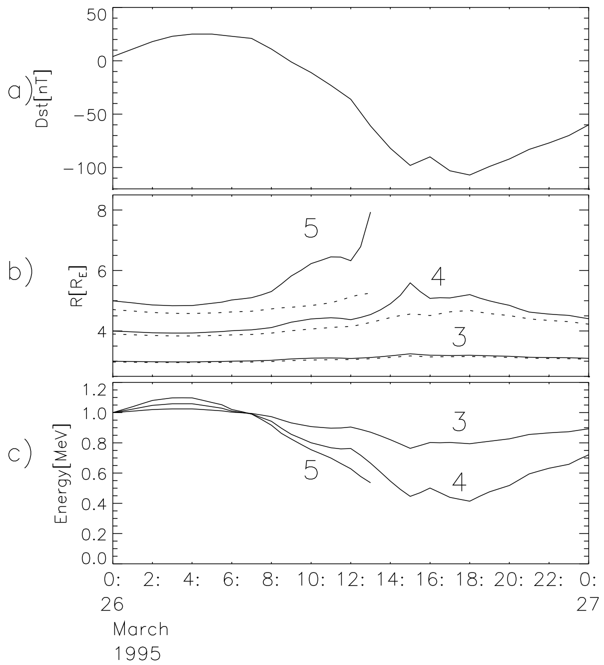
a)
Dst[nT]
50
0
−50
−100
b)
R[R_E]
8
6
4
5
4
3
c)
Energy[MeV]
1.2
1.0
0.8
0.6
0.4
0.2
0.0
3
5
4
0: 2: 4: 6: 8: 10: 12: 14: 16: 18: 20: 22: 0:
26
March
1995
27

Figure 3

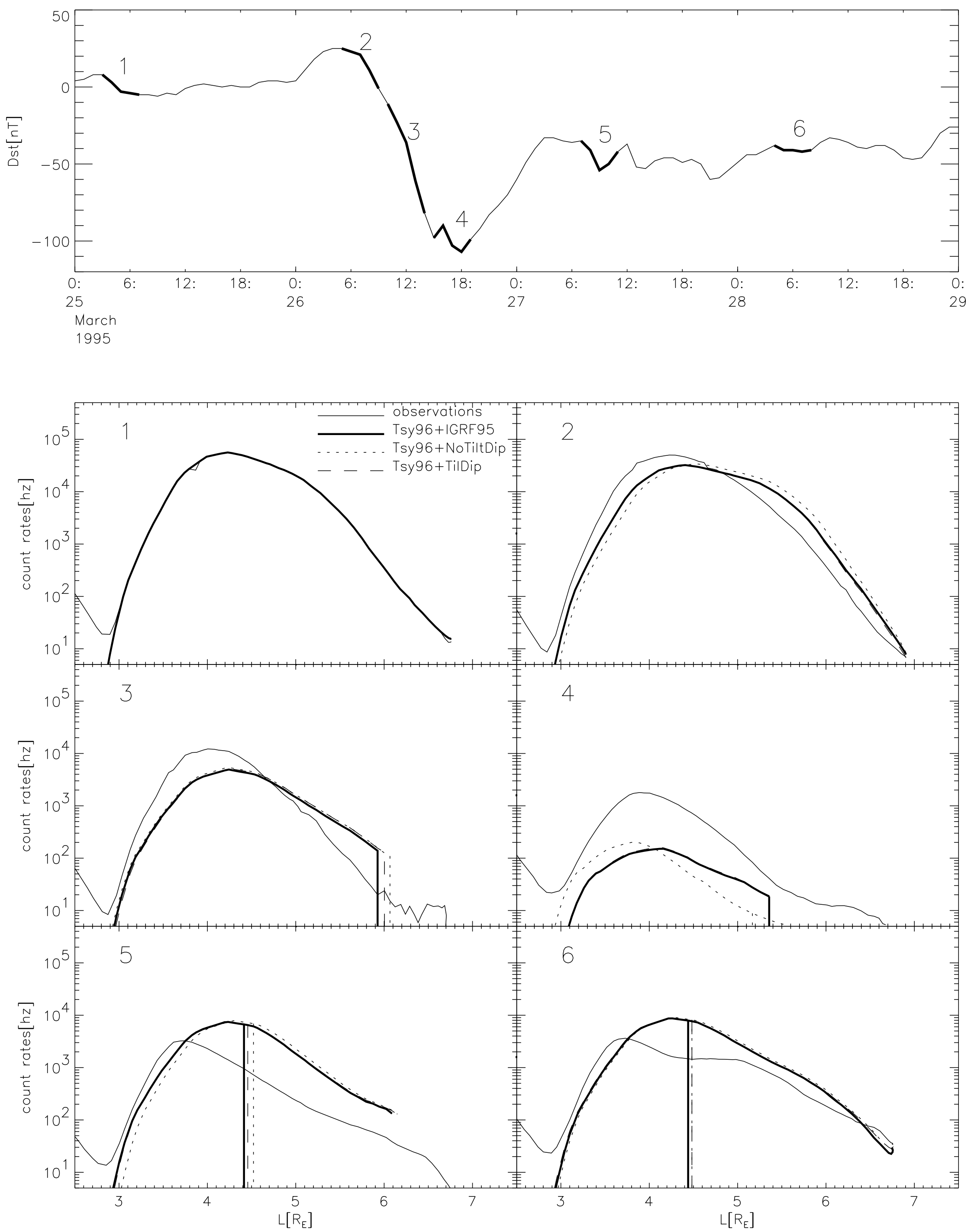

50
0
−50
−100
Dst[nT]
1
2
3
4
5
6
0:
6:
12:
18:
25
March
1995
26
27
28
29
observations
Tsy96+IGRF95
Tsy96+NoTiltDip
Tsy96+TilDip
count rates[hz]
L[R_E]

Figure 4

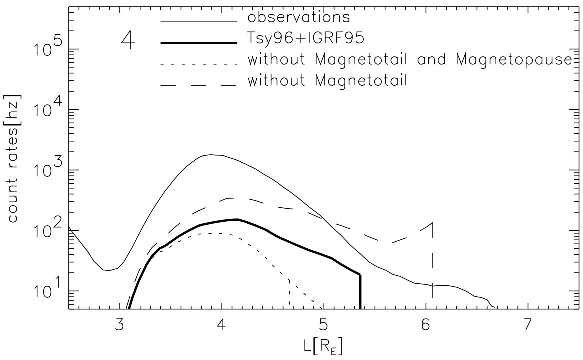
4
observations
Tsy96+IGRF95
without Magnetotail and Magnetopause
without Magnetotail
count rates[hz]
10^5
10^4
10^3
10^2
10^1
3
4
5
6
7
L[R_E]

Figure 5

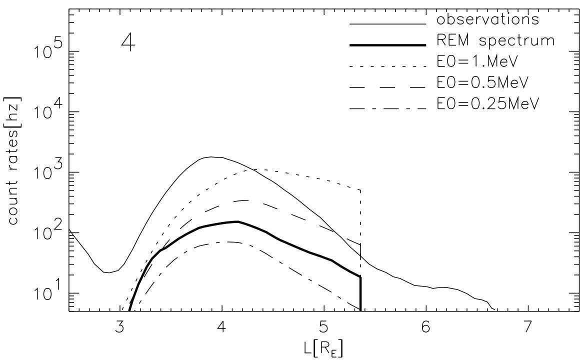
4
observations
REM spectrum
E0=1.MeV
E0=0.5MeV
E0=0.25MeV
count rates[hz]
10^5
10^4
10^3
10^2
10^1
3
4
5
6
7
L[R_E]

Figure 6

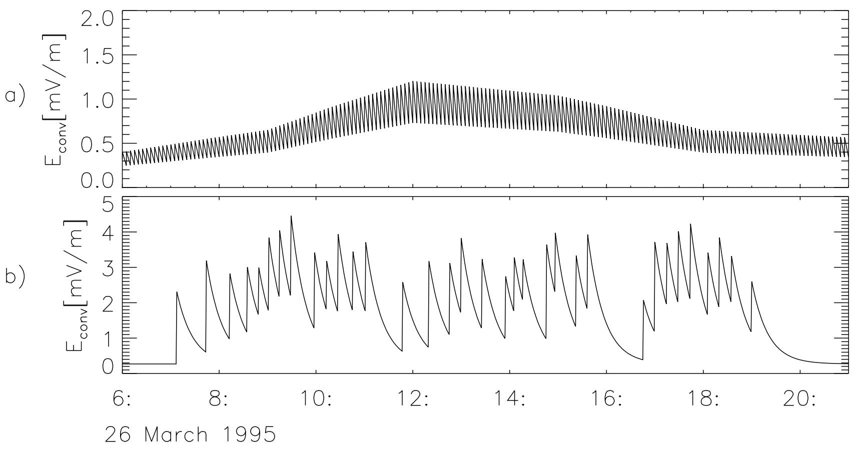
a)
b)
E_{conv}[mV/m]
2.0
1.5
1.0
0.5
0.0
5
4
3
2
1
0
6:
8:
10:
12:
14:
16:
18:
20:
26 March 1995

Figure 7

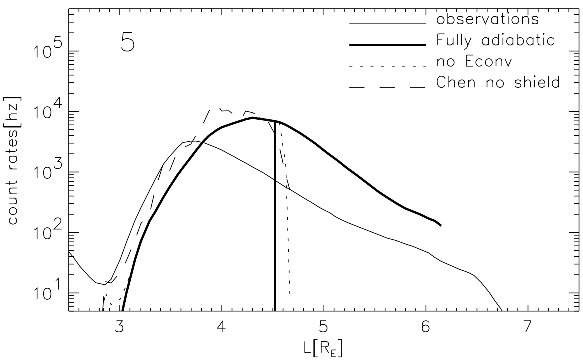
observations
Fully adiabatic
no Econv
Chen no shield
5
count rates[hz]
L[R_E]

Figure 8

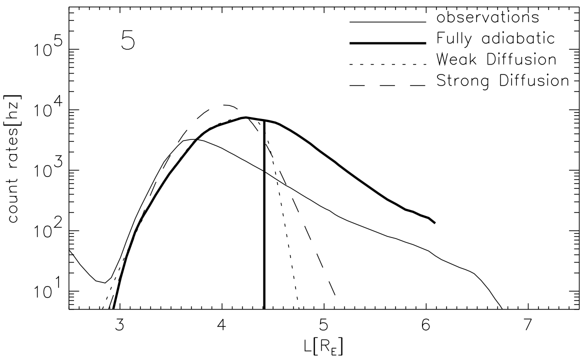
5
observations
Fully adiabatic
Weak Diffusion
Strong Diffusion
count rates[hz]
10^5
10^4
10^3
10^2
10^1
3
4
5
6
7
L[R_E]

Figure 9

Supplemental Abstract for *JGR–Space Physics* Manuscripts

2000JA900060

In this paper we study the variation of the relativistic electron fluxes in the Earth's outer radiation belt during the March 26, 1995, magnetic storm. Using observations by the radiation environment monitor (REM) on board the space technology research vehicle (STRV-1b), we discuss the flux decrease and possible loss of relativistic electrons during the storm main phase. In order to explain the observations we have performed fully adiabatic and guiding center simulations for relativistic equatorial electrons in the nonstationary Tsyganenko96 magnetospheric magnetic field model. In our simulations the drift of electrons through the magnetopause was considered as a loss process. We present our model results and discuss their dependence on the magnetospheric magnetic and electric field model, as well as on the prestorm fluxes used in the simulations.

DESORGHER ET AL.: MAGNETIC STORM SIMULATIONS

DESORGHER ET AL.: MAGNETIC STORM SIMULATIONS

DESORGHER ET AL.: MAGNETIC STORM SIMULATIONS

DESORGHER ET AL.: MAGNETIC STORM SIMULATIONS

DESORGHER ET AL.: MAGNETIC STORM SIMULATIONS

DESORGHER ET AL.: MAGNETIC STORM SIMULATIONS

DESORGHER ET AL.: MAGNETIC STORM SIMULATIONS

DESORGHER ET AL.: MAGNETIC STORM SIMULATIONS

DESORGHER ET AL.: MAGNETIC STORM SIMULATIONS

DESORGHER ET AL.: MAGNETIC STORM SIMULATIONS

DESORGHER ET AL.: MAGNETIC STORM SIMULATIONS

DESORGHER ET AL.: MAGNETIC STORM SIMULATIONS

DESORGHER ET AL.: MAGNETIC STORM SIMULATIONS

DESORGHER ET AL.: MAGNETIC STORM SIMULATIONS

DESORGHER ET AL.: MAGNETIC STORM SIMULATIONS

DESORGHER ET AL.: MAGNETIC STORM SIMULATIONS

DESORGHER ET AL.: MAGNETIC STORM SIMULATIONS

DESORGHER ET AL.: MAGNETIC STORM SIMULATIONS

DESORGHER ET AL.: MAGNETIC STORM SIMULATIONS

DESORGHER ET AL.: MAGNETIC STORM SIMULATIONS

DESORGHER ET AL.: MAGNETIC STORM SIMULATIONS

DESORGHER ET AL.: MAGNETIC STORM SIMULATIONS

DESORGHER ET AL.: MAGNETIC STORM SIMULATIONS

DESORGHER ET AL.: MAGNETIC STORM SIMULATIONS

DESORGHER ET AL.: MAGNETIC STORM SIMULATIONS

DESORGHER ET AL.: MAGNETIC STORM SIMULATIONS

DESORGHER ET AL.: MAGNETIC STORM SIMULATIONS

DESORGHER ET AL.: MAGNETIC STORM SIMULATIONS

DESORGHER ET AL.: MAGNETIC STORM SIMULATIONS

DESORGHER ET AL.: MAGNETIC STORM SIMULATIONS

DESORGHER ET AL.: MAGNETIC STORM SIMULATIONS

DESORGHER ET AL.: MAGNETIC STORM SIMULATIONS

DESORGHER ET AL.: MAGNETIC STORM SIMULATIONS

DESORGHER ET AL.: MAGNETIC STORM SIMULATIONS

DESORGHER ET AL.: MAGNETIC STORM SIMULATIONS

DESORGHER ET AL.: MAGNETIC STORM SIMULATIONS

DESORGHER ET AL.: MAGNETIC STORM SIMULATIONS

DESORGHER ET AL.: MAGNETIC STORM SIMULATIONS

DESORGHER ET AL.: MAGNETIC STORM SIMULATIONS

DESORGHER ET AL.: MAGNETIC STORM SIMULATIONS

DESORGHER ET AL.: MAGNETIC STORM SIMULATIONS

DESORGHER ET AL.: MAGNETIC STORM SIMULATIONS

DESORGHER ET AL.: MAGNETIC STORM SIMULATIONS

DESORGHER ET AL.: MAGNETIC STORM SIMULATIONS

DESORGHER ET AL.: MAGNETIC STORM SIMULATIONS

DESORGHER ET AL.: MAGNETIC STORM SIMULATIONS

DESORGHER ET AL.: MAGNETIC STORM SIMULATIONS

DESORGHER ET AL.: MAGNETIC STORM SIMULATIONS

DESORGHER ET AL.: MAGNETIC STORM SIMULATIONS

DESORGHER ET AL.: MAGNETIC STORM SIMULATIONS

DESORGHER ET AL.: MAGNETIC STORM SIMULATIONS

DESORGHER ET AL.: MAGNETIC STORM SIMULATIONS

DESORGHER ET AL.: MAGNETIC STORM SIMULATIONS

DESORGHER ET AL.: MAGNETIC STORM SIMULATIONS

DESORGHER ET AL.: MAGNETIC STORM SIMULATIONS

DESORGHER ET AL.: MAGNETIC STORM SIMULATIONS

DESORGHER ET AL.: MAGNETIC STORM SIMULATIONS

DESORGHER ET AL.: MAGNETIC STORM SIMULATIONS

DESORGHER ET AL.: MAGNETIC STORM SIMULATIONS

DESORGHER ET AL.: MAGNETIC STORM SIMULATIONS

DESORGHER ET AL.: MAGNETIC STORM SIMULATIONS

DESORGHER ET AL.: MAGNETIC STORM SIMULATIONS

DESORGHER ET AL.: MAGNETIC STORM SIMULATIONS

DESORGHER ET AL.: MAGNETIC STORM SIMULATIONS

DESORGHER ET AL.: MAGNETIC STORM SIMULATIONS

DESORGHER ET AL.: MAGNETIC STORM SIMULATIONS

DESORGHER ET AL.: MAGNETIC STORM SIMULATIONS

DESORGHER ET AL.: MAGNETIC STORM SIMULATIONS

DESORGHER ET AL.: MAGNETIC STORM SIMULATIONS